IOPscience iopscience.iop.org

Home Search Collections Journals About Contact us My IOPscience

A simple energy filter for low energy electron microscopy/photoelectron emission microscopy instruments

This article has been downloaded from IOPscience. Please scroll down to see the full text article.

2009 J. Phys.: Condens. Matter 21 314007

(http://iopscience.iop.org/0953-8984/21/31/314007)

View the table of contents for this issue, or go to the journal homepage for more

Download details:
IP Address: 129.252.86.83
The article was downloaded on 29/05/2010 at 20:39

Please note that terms and conditions apply.

IOP PUBLISHING JOURNAL OF PHYSICS: CONDENSED MATTER

J. Phys.: Condens. Matter **21** (2009) 314007 (13pp) doi:10.1088/0953-8984/21/31/314007

A simple energy filter for low energy electron microscopy/photoelectron emission microscopy instruments

R M Tromp[1], Y Fujikawa[2], J B Hannon[1], A W Ellis[1], A Berghaus[3] and O Schaff[3]

[1] IBM Research Division, T J Watson Research Center, PO Box 218, 1101 Kitchawan Road, Yorktown Heights, NY 10598, USA
[2] Institute for Materials Research, Tohoku University, Sendai 980-8577, Japan
[3] SPECS GmbH, Voltastraße 5, D-13355 Berlin, Germany

Received 5 January 2009, in final form 23 March 2009
Published 7 July 2009
Online at stacks.iop.org/JPhysCM/21/314007

Abstract

Addition of an electron energy filter to low energy electron microscopy (LEEM) and photoelectron emission microscopy (PEEM) instruments greatly improves their analytical capabilities. However, such filters tend to be quite complex, both electron optically and mechanically. Here we describe a simple energy filter for the existing IBM LEEM/PEEM instrument, which is realized by adding a single scanning aperture slit to the objective transfer optics, without any further modifications to the microscope. This energy filter displays a very high energy resolution $\Delta E/E = 2 \times 10^{-5}$, and a non-isochromaticity of $\sim$0.5 eV/10 μm. The setup is capable of recording selected area electron energy spectra and angular distributions at 0.15 eV energy resolution, as well as energy filtered images with a 1.5 eV energy pass band at an estimated spatial resolution of $\sim$10 nm. We demonstrate the use of this energy filter in imaging and spectroscopy of surfaces using a laboratory-based He I (21.2 eV) light source, as well as imaging of Ag nanowires on Si(001) using the 4 eV energy loss Ag plasmon.

1. Introduction

Over the last decade, energy filtering has become an important ingredient in many electron microscopy studies, both in biology and in materials science. The transmission electron microscope (TEM) in particular has benefited from the development of advanced energy filters that enable the recording of selected area energy spectra, as well as energy filtered diffraction patterns and images. Several excellent textbooks are testament to the maturity of this field [1]. Low energy electron microscopy (LEEM) and photoelectron microscopy (PEEM) are relative newcomers to the electron microscopy family [2]. Worldwide, there are fewer than 30 LEEM/PEEM instruments, and no more than half of these are equipped with an energy filter.

In virtually all energy filtered electron microscopes the energy filtering function is incorporated by insertion of an energy dispersive element which deflects the electron away from the main optical axis of the microscope, the only exception being the Wien filter which is not used very widely. Common examples are omega and alpha filters, pioneered by Krahl and Rose in the context of the TEM [1], the Gatan post-column energy filter [3], and the hemispherical analyzer in the case of LEEM/PEEM [4]. All of these systems are quite complex as a result of the electron optical requirements. Here we will not review the design and properties of energy filters used in transmission electron microscopes. Instead we will restrict ourselves to LEEM/PEEM instruments.

The simplest energy filter available today in a commercial PEEM instrument (Omicron Focus PEEM) is a retarding fine mesh filter just in front of the final image intensifier. Such a filter transmits electrons whose energy exceeds the retarding potential applied to the mesh, i.e. it is a high-pass filter. While simple, there are obvious disadvantages. To obtain a spectrum, the pass energy has to be scanned, and the signal intensity in the image must be differentiated with respect to the scan voltage. The signal-to-noise ratio is not as good as that obtained with a band-pass filter, and the energy resolution is limited by the non-uniform fields associated with a mesh [5]. A more commonly used solution is the

 © 2009 IOP Publishing Ltd Printed in the UK

insertion of a hemispherical analyzer in the electron optical path. Hemispherical analyzers have a long history in electron spectroscopy, particularly in photoelectron spectroscopy. They can provide outstanding energy resolution (below 1 meV in the most advanced photoelectron spectrometers today [6]), and their properties are well understood. However, the analyzer by itself does not quite do the job. It must be coupled to the rest of the optical system by coupling lenses, and usually the pass energy of the electrons must be reduced from the column energy of 15–20 keV to a much lower value of several 100 eV to obtain the desired energy resolution, requiring retarding/accelerating lenses at the input/output of the analyzer. In the usual setup the entrance slit of the analyzer is imaged and dispersed onto the exit slit. Due to symmetry, the midplane of the analyzer (halfway between the entrance and exit planes) is achromatic. Thus, if we desire to energy filter the image, the image plane is projected onto the midplane of the analyzer, while the diffraction plane is projected onto the entrance plane, and then imaged and dispersed onto the exit plane by the analyzer. Slits in the entrance and exit planes then define and select the energy (and momentum) range of interest, and the energy filtered image can be magnified onto the viewing screen. If the exit slit is removed, the energy spectrum can be directly seen in the diffraction plane and imaged onto the viewing screen. Energy filtered electron angular distributions can also be obtained, but this requires a very different setup [4]. Now the diffraction plane must be projected onto the midplane of the analyzer, while the image plane is projected on the analyzer entrance plane and then imaged and dispersed onto the exit plane. That is, image and diffraction planes swap places when going from energy filtered imaging to energy filtered diffraction. This requires the presence of additional coupling lenses at the analyzer entrance. As the electron optical axis makes a 180° turn through the analyzer, alignment of the system can the tricky. An instrument using two hemispherical analyzers in series to compensate for filtering aberrations was introduced a few years ago [7].

Following TEM energy filter designs, the SMART machine incorporates an omega filter [8]. Such a design has several advantages. It operates at full electron beam energy, i.e. the electrons are not retarded inside the analyzer. The electron energy resolution is excellent ($\Delta E/E \sim 2 \times 10^{-5}$). Since the optical axes before and after the analyzer are in line, the filter can be bypassed by turning the deflection fields off, which is useful in microscope alignment. However, as in the case of the spherical analyzer, special coupling lenses are still required, and design and construction of the omega filter is complex, and the equipment is bulky and expensive.

In order to simplify the design and construction of energy filtered LEEM/PEEM instruments, and to ease microscope alignment, we have searched for an energy filter solution that can be installed with a minimum effort and expense, while still providing high quality spectroscopic performance. It was our goal to utilize as much as possible microscope components already part of a typical LEEM/PEEM instrument, and to not unnecessarily introduce new optical components that might complicate microscope operation. Of course, there is a need for a dispersive element somewhere along the optical path. One option would be to include a traditional energy filter such as a hemisphere or omega filter. However, the complexity of such a solution acted as a powerful deterrent. An in-line solution such as a Wien filter was another possibility, but the relatively poor optical quality of a Wien filter, associated with the difficulty of adequately controlling fringe fields also made this option less than attractive.

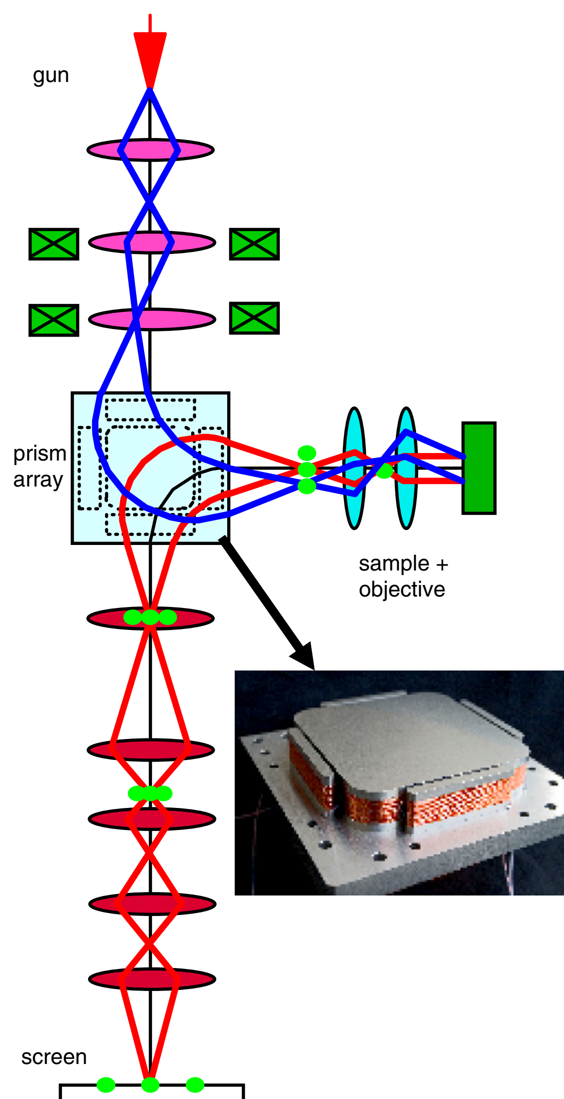

Figure 1. Schematic diagram of the IBM LEEM/PEEM system. At the center of the instrument is the magnetic prism array that deflects the electron beam from the gun towards the sample, and after reflection from the sample to the projector column. The ray paths shown are for dark field (i.e. off-axis) illumination (blue rays). An on-axis beam is selected for imaging (red rays). The projector column is set to display the low energy electron diffraction pattern on the image screen. A photograph of one of the two parallel prism array plates is shown in the inset. A flux closure ring surrounding the active polepieces equipped with copper windings was removed for this photograph.

2. A new and simple energy filter

A simple and obvious solution offers itself by careful consideration of the structure of the existing IBM LEEM/PEEM instrument (figure 1). A cold field emission gun (the top end

of a Hitachi SEM) delivers a 15 keV electron beam. The combination of a gun lens and a condenser lens, together with a triplet of steering coils provides the beam control necessary for correct sample illumination. At the center of the microscope we find a square magnetic prism array [9]. The function of this device is to spatially separate the condenser column from the projector column. It deflects the beam by 90° into the objective lens system. Between the objective lens and the sample, the beam is decelerated to an energy in the range of 0–100 eV by applying a negative potential to the sample. The field strength between objective lens and sample is ∼100 kV cm^{-1}. After reflection from the sample the electron beam is accelerated back to 15 keV and re-enters the objective lens. Therefore, in the objective lens system the incident and reflected paths coincide spatially. The prism array then deflects the reflected electrons down into the projector column where the sample image as well as the diffraction pattern can be magnified onto the channelplate intensified viewing screen.

It will be illustrative to take a closer look at the optical properties of the prism array. Geometrically, the prism array consists of a number of magnetic prisms that serve to both deflect and focus the electrons as they pass through. The simplest setup might be a square or circular dipole, consisting of two parallel square or circular magnetic pole plates excited by an electromagnetic coil. However, this has significant disadvantages. A magnetic dipole field focuses electrons that move in a plane normal to the magnetic field, but there is no focusing in the direction parallel to the magnetic field. Thus, a simple dipole field cannot act as a double-focusing image forming element in an electron microscope. More complex systems, consisting of an array of dipole fields, with the array elements excited at different magnetic field strengths, were first introduced by Kolarik *et al* [9], as a versatile image forming deflection element in a low energy electron microscope. Later, Rose *et al* [10] showed that a central square dipole magnet at one fixed magnetic potential, surrounded by a second square ring at a second magnetic potential, can behave like a combination of round lenses. In the present configuration the outer ring (inside a flux closure ring) is subdivided into four segments, one for each quadrant, to provide fine-adjustment capabilities for each of the four quadrants. Figure 2(a) contains the key optical results [11]. Plotted are the image distance as function of object distance. Both are referenced to the center of the groove between the outer magnetic sector and the magnetic flux closure ring surrounding the prism array. The plot is divided in four quadrants. The lower left quadrant corresponds to object/image locations inside the prism array. The upper right quadrant corresponds to object/image locations outside the array. The red/black dashed lines in both quadrants show the results of the imaging simulations for the prism array used in the IBM LEEM/PEEM instrument. In fact, the curves show overlapped results for in-plane imaging (black) and out-of-plane imaging (red). Remarkably, the calculated focusing locations are identical for in-plane and out-of-plane focusing, for any object position. In other words, for any object location the prism array forms a stigmatic image in the corresponding image plane. In general this is not necessarily the case, and it is not the case with the prism arrays incorporated

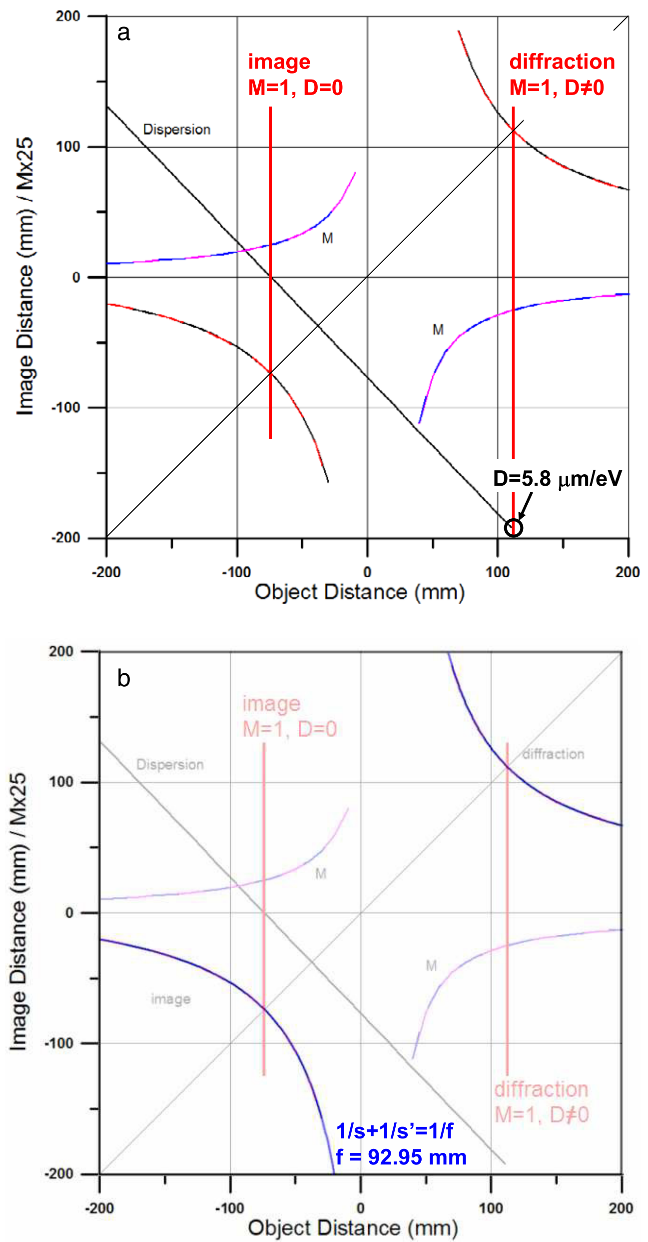

Figure 2. (a) Theoretical prism array properties. Plotted are image distances versus object distances, referenced to the center of the groove between the outer polepiece and the flux closure ring of the prism array. Red/black lines are for in-plane and out-of-plane focusing. Both focusing conditions overlap everywhere. Pink/blue lines show the corresponding magnifications M, which also overlap everywhere, indicating stigmatic imaging properties at all object/image combinations. This property is only fulfilled for a specific set of prism array dimensions and magnetic excitations. Finally, the solid black line shows the dispersion D. An intermediate image is placed on the diagonal of the prism array, where $M = 1$, and $D = 0$, guaranteeing that the image is dispersion free. Diffraction planes are located symmetrically, outside the prism array, again with $M = 1$, and a calculated dispersion of 5.8 μm eV^{-1} for 15 keV electrons. The measured dispersions is 6 μm eV^{-1}, in good agreement with theory. (b) A simple thin lens approximation, $1/s + 1/s' = 1/f$, with $f = 92.95$ mm was used to calculate the solid blue lines. They overlap perfectly with the full calculations for object/image positions shown in (a), indicating that the prism array can be treated like an ideal thin lens in terms of its imaging properties, greatly easing integration of this rather complex compound optical element in the LEEM optical column.

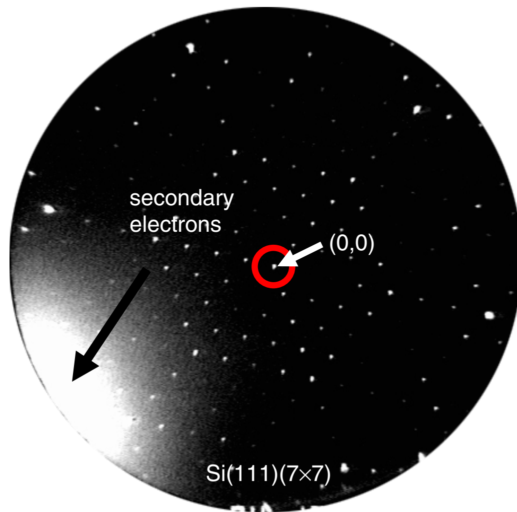

Figure 3. LEED pattern of a Si(111)-(7 × 7) surface. The (0, 0) beam is on the optical axis, while the secondary electron cloud (arrow) is deflected away from the optical axis due to chromatic dispersion of the prism array. The red circle indicates a typical contrast aperture used in imaging. The secondary electrons are not transmitted by the aperture.

in most LEEM/PEEM instruments with deflection angles of 60°. Also plotted in figure 2 (pink/blue dashed lines) are the magnifications M for in-plane and out-of-plane focusing, which again overlap. Of special significance are the locations for which $M = 1$. There is one such location outside the prism array, and a second location inside the prism array on the diagonal plane. From the distance between the loci with $M = 1$ we readily derive a focal length of the prism array of 92.95 mm. While the prism array looks nothing like a thin lens, it is still instructive to compare its optical performance with that of a thin lens. In figure 2(b), the blue line overlapping the red–black dashed lines is calculated using the simplest possible thin lens formula, i.e. $1/s + 1/s' = 1/f$, with $f = 92.95$ mm. The agreement is rather astonishing. This square prism array really behaves like a single, classical thin lens, greatly simplifying its incorporation in a microscope design.

Finally, figure 2(a) plots the chromatic dispersion (black line). The dispersion is zero on the diagonal plane of the prism. In order to assure that image quality is not negatively affected by chromatic dispersion, an intermediate image is placed on this prism diagonal. On the objective lens side, the diffraction plane is located outside the prism array, and re-imaged on the projector side, at a magnification $M = 1$. That is, the entrance and exit diffraction patterns are located symmetrically about the prism array. Importantly, the chromatic dispersion is now not equal to zero. Upon transfer of the diffraction pattern from the objective side to the projector side, the diffraction pattern is chromatically dispersed. This is a fact well known, and readily seen in a typical LEED pattern where the secondary electrons are dispersed away from the optical axis (figure 3). When a contrast aperture is placed on the center LEED spot (indicated by the red circle in figure 3), as usual in both bright field and dark field LEEM imaging experiments, the secondary electrons are automatically ‘filtered out’, and in this sense all LEEM experiments are performed in a rough energy filtered mode. The dispersion is not insignificant: the theoretical value in the exit diffraction plane is $\sim$5.8 μm eV^{-1}, compared to a measured value of $\sim$6 μm eV^{-1}, at 15 keV electron energy. To get a better feeling for this number, we can derive a simple formula for the dispersion, using elementary considerations. With a main deflection radius, R, inside the prism array (neglecting the fact that the narrow outer segments have a somewhat different deflection radius), with a deflection angle of 90°, and a distance from the edge of the other prism segment to the diffraction plane, L, and an electron energy E inside the prism array, we find that the dispersion in the diffraction plane is given by $D = (R + L)/2E$. For the geometry of the present prism array, this yields a dispersion of 6.1 μm eV^{-1}, very close to the full theory and to the experiment. This can be compared to a hemispherical analyzer with a deflection radius R, and a deflection angle of 180°, for which the dispersion is $D = 2R/E$. For the same deflection radius R, a hemispherical analyzer yields a dispersion of 10 μm eV^{-1}, about twice as large as the prism array. This is reasonable as the total deflection angle is twice as large (180° versus 90°).

Given that the LEEM/PEEM instrument already contains this integral, in-line dispersive element, the question naturally presents itself: can we use this as the energy filter? Only one element is missing: an entrance slit in the diffraction plane on the objective lens side of the prism array that will define the energy resolution of the filter. The required width of the slit is obtained from the dispersion. For a desired energy resolution of 0.25 eV at 15 keV pass energy with a dispersion of 6 μm eV^{-1}, the required slit width is 1.5 μm. Such a slit would be used for obtaining high resolution energy spectra. For imaging applications one may prefer to use a larger slit that passes the peak in a valence band or core level spectrum over its full natural width. For instance, a 10 μm slit passes an energy window of $\sim$1.6 eV, while a 20 μm slit passes a width of $\sim$3.3 eV. These two aperture sizes are also used for routine LEEM imaging experiments, so that there is a good match between imaging and filtering requirements. We have installed entrance slits in the diffraction plane on the objective lens side of the prism array, with widths of 1.5, 10 and 20 μm, and a length of 1 mm. They were fabricated by ion beam milling. A suitable membrane was formed by taking a Si wafer with a 1 μm thick Si_3N_4 film on one side of the wafer. A 1.5 × 0.5 mm^2 rectangle was defined on the back of the wafer by lithographic means, and an opening created by anisotropic etching. Etching stopped at the Si_3N_4 thin film, leaving behind a thin Si_3N_4 membrane. This membrane was then covered with a thin Cr adhesion layer, followed by $\sim$1 μm of Au, both deposited on both sides of the wafer and the membrane. A single Si chip, size 3 × 3 mm^2 contained 4 such membranes. Focused ion beam (FIB) milling with Ga ions was then used to define three slits, with widths of 1.5, 10 and 20 μm and lengths of 1 mm, as discussed above, as well as a pattern of square 5 × 5 μm^2 holes for alignment and focusing purposes. This aperture chip was next mounted onto a seesaw motion mechanism that provides mechanical stiffness and reduces the risk of mechanical vibration, and mounted inside a newly constructed objective transfer lens. The seesaw

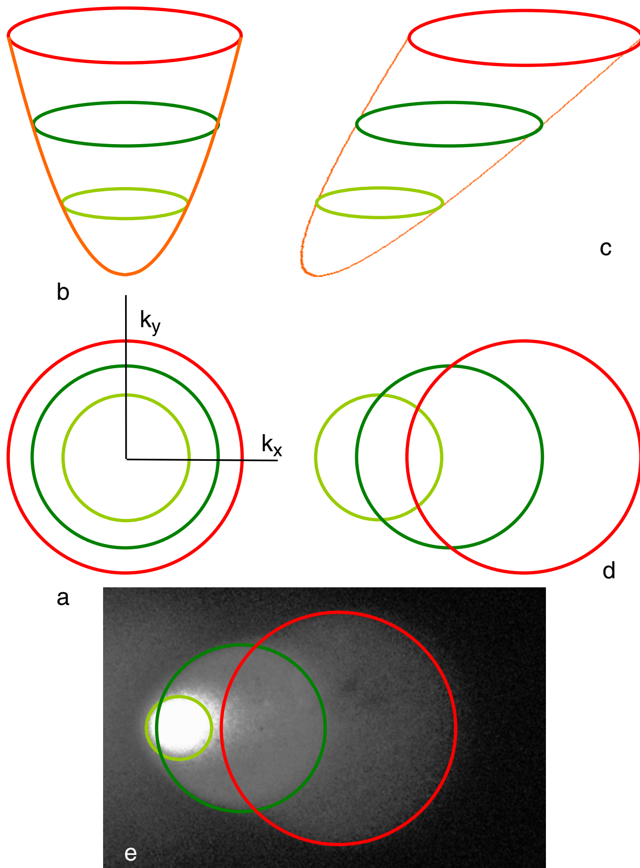

Figure 4. (a) In the backfocal plane on the entrance side of the prism array, the angular distributions of electrons with different energies (red, dark green, light green, from highest energy to lowest) are imaged as concentric circular regions representing their (k_x, k_y) momentum distributions. (b) We can represent this in a (k_x, k_y, E) paraboloid of revolution, with the vertical axis representing energy. (c) After passage through the prism array this energy axis is skewed due to dispersion. (d) Projecting this skewed paraboloid back in the diffraction plane on the exit side of the prism array, the red, dark green and light green circles are now shifted relative to each other. (e) Experimental example of such a dispersed distribution.

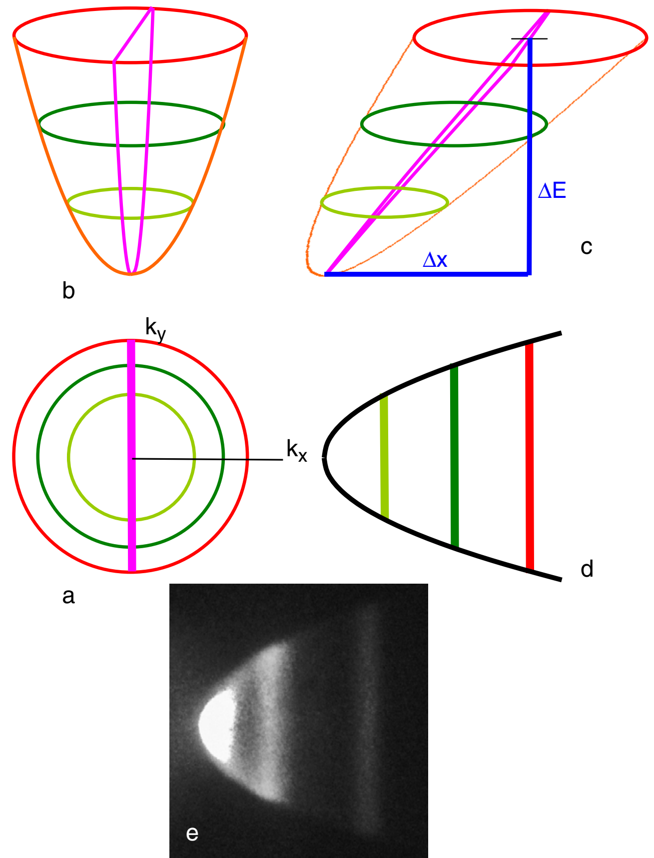

Figure 5. Schematic view of prism dispersion with an entrance slit placed across the center of the angular distribution. (a) Location of the entrance slit is indicated by the purple line. (b) This corresponds to a slice through the center of the paraboloid. (c) After passage through the prism array this slice is skewed, along with the full paraboloid. The ratio $\Delta x/\Delta E$ defines the dispersion of the spectrometer. (d) After projection into the backfocal plane on the exit side of the prism array, the slice corresponds to a (k_y, E) spectrum at $k_x = 0$, where the different energies now correspond to lines. The black bounding line is a parabola. (e) Experimental example after insertion of an entrance slit in the spectrum shown in figure 4(a).

is connected to an external micrometer drive through miniature vacuum bellows. For non-filtered operation the apertures can be retracted fully from the optical path. For energy filtered operation the desired slit is inserted in the path of the electrons, in the objective-lens-side diffraction plane of the prism array.

3. Spectroscopy, imaging, and diffraction

To fully understand how the energy filter works, it is useful to review the basics with the aid of figure 4. For illustrative purposes, let us consider three electron energies $E_1 < E_2 < E_3$. The backfocal plane of the objective lens, and the conjugate diffraction plane at the entrance of the prism array, contain the angular distributions (k_x, k_y) of electrons coming from the sample. For isotropic emission, this gives rise to circular discs, with the radius of each disc R_i proportional to the square root of the energy. These discs are direct maps of the electron distribution in the (k_x, k_y) plane, and the discs for different electron energies are concentric (figure 4(a)). Of course, we can also plot (k_x, k_y) versus energy, giving rise to the paraboloid of revolution in figure 4(b). After passage through a dispersive field, (k_x, k_y) discs at different energies will be displaced relative to each other. As dispersion is to first order linear in energy, this corresponds to a skew of the (k_x, k_y) versus E paraboloid in the dispersive direction (figure 4(c)). Projecting this figure back onto a single plane (i.e. the diffraction plane on the exit side of the prism array), the (k_x, k_y) discs at different energies are now linearly dispersed relative to each other (figure 4(d)). Figure 4(e) shows an experimental result obtained with photoemitted electrons excited with a He I/II discharge lamp, which shows a distribution very similar to figure 4(d).

We immediately see the dispersion, but (k_x, k_y) discs for different energies are now shifted relative to each other and overlapped in a single plane. This is why we must insert a slit in the (k_x, k_y) plane on the entrance side of the prism array. This is illustrated for a slit inserted across the center of the (k_x, k_y) discs (figure 5(a)). This slit takes a slice out of the (k_x, k_y)

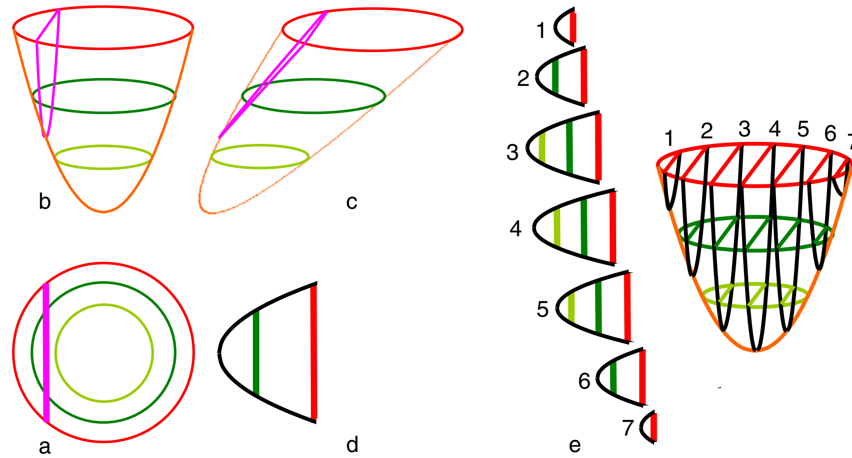

Figure 6. Schematic view of prism dispersion with an entrance slit placed off-center relative to the angular distribution. (a) Off-center location of the entrance slit is indicated by the purple line. (b) This corresponds to an off-center slice through the paraboloid. (c) After passage through the prism array this slice is skewed, along with the full paraboloid. (d) After projection into the backfocal plane on the exit side of the prism array, the slice corresponds to a (k_y, E) spectrum at $k_x \neq 0$, where the different energies again correspond to lines. The black bounding line is again a parabola. Notice that the lowest energy (light green) now falls outside the aperture and does not show up in the energy spectrum in (d). (e) Reconstruction of (k_x, k_y, E) paraboloid by scanning the entrance slit and obtaining a (k_y, E) spectrum for each slit position. While shown here for only 7 entrance slit positions, a much finer resolved dataset can be obtained by increasing the number of slices. For example, in figures 14 and 15, about 120 entrance slit positions were used.

versus E paraboloid in figure 5(b), and this slice is dispersed by the prism array in figure 5(c). After back projection onto the dispersive plane after passage through the prism array we obtain an energy spectrum that contains E along the horizontal axis, and k_y along the vertical axis. As k is proportional to the square root of E, the boundary of the dispersion figure is parabolic. The three energy discs in figure 5(a) now give rise to distinct lines in the energy spectrum of figure 5(d). An experimental result using the same conditions as in figure 4(e), but now with a slit, is shown in figure 5(e). An energy filtered real-space image can be obtained by inserting a contrast aperture at the desired electron energy and (k_x, k_y) in the energy spectrum of figure 5(e), excluding all other energy and k values, and magnifying the corresponding image on the viewing screen. We will return to this later.

Using this simple setup we can obtain energy spectra, as well as energy filtered images. But how can we obtain energy filtered diffraction patterns? Recall that in the usual energy filtered LEEM/PEEM setups with hemispherical analyzers, the analyzer is preceded by a set of special coupling lenses. For energy filtered imaging, the image is located at the center of the hemisphere, with diffraction planes located on the entrance and exit planes. Conversely, for energy filtered diffraction, the locations of image and diffraction planes are swapped, with the diffraction plane now at the center of the hemisphere, and the image on the entrance and exit planes. In the setup discussed so far, utilizing the prism array as an energy filter, we have made no provisions for additional lenses that can swap the locations of image and diffraction planes. Can we then still obtain energy filtered diffraction patterns? The answer is yes, and it does not require the use of additional optical elements. Let us go back to figure 5. The energy spectrum in figure 5(d) is a figure of k_y versus E, for a particular choice of k_x (in this case $k_x = 0$). But we are perfectly free to make other choices of k_x. Figure 6 shows an example where we have placed the entrance slit off-center on the entrance side of the prism array (figure 6(a)). Again we take a slice out of the (k_x, k_y) versus E paraboloid (figure 6(b)), which gets dispersed in the usual manner (figure 6(c)), and projected down onto the exit plane (figure 6(d)). In figure 6(d) we simply see a slice out of the (k_x, k_y) versus E paraboloid of figure 6(b), at a different value of k_x. Of course we can do this for any choice of k_x. In fact, if we were to scan the entrance slit across the entrance plane (figure 6(a)), and obtain an energy spectrum for each slit position (figure 6(d)), we can reconstruct the full (k_x, k_y) versus E paraboloid. This is by mechanically scanning the slit across the entrance plane, and recording the energy spectrum for each setting. This is illustrated in figure 6(e), where a set of 7 energy spectra, obtained at different entrance slit positions, are used to reconstruct the 3D paraboloid. Of course, at only 7 slices this reconstruction is very coarse. In comparison, the data presented in figures 14 and 15 were obtained with ∼120 entrance slit positions to achieve a much higher resolution reconstruction. With such a dataset we can take any cut through the (k_x, k_y) versus E paraboloid. A vertical cut through the center (figure 4(b)) gives us a k_y versus E energy spectrum at $k_x = 0$. On the other hand, a horizontal slice at a fixed energy gives the electron density in the (k_x, k_y) plane at that energy, i.e. an energy filtered diffraction pattern. We can also take cuts at fixed k_y, or indeed any other cut we might like. Such a full dataset obtained in a valence band photoemission experiment will contain the electronic band dispersion data, Fermi surfaces, electron energy distributions at fixed (k_x, k_y) (a vertical line cut through the paraboloid), etc. So in many ways, this simple method of acquiring data is complementary to the usual method of taking energy filtered diffraction data. In the

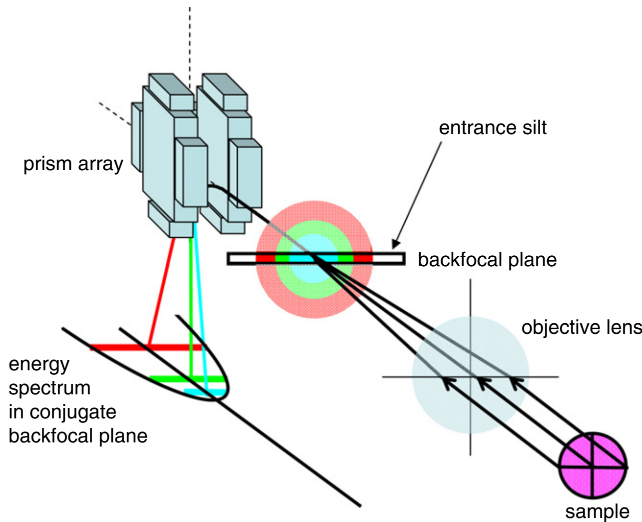

Figure 7. Three-dimensional schematic of the energy filter setup. Parallel electron trajectories leaving the sample cross over in the backfocal plane, which is the entrance plane to the prism array spectrometer. An entrance slit selects a narrow slice out of the 2D angular distribution. After deflection through the prism array, a (k_y, E) spectrum is observed in the exit plane. The objective lens system in the actual microscope consists of an objective lens plus a transfer lens (see figure 1). For simplicity, it is represented here by a single objective lens.

latter method the full (k_x, k_y) versus E paraboloid can also be reconstructed, this time by scanning the filtering energy. The advantage of the present method is that addition of a scanning slit is much simpler and less expensive than the addition of several electron lenses to facilitate the swapping of image and diffraction planes in and around the energy filter.

Notice that the considerations of figures 4–6 do not depend on the exact design of the energy filter, implying that a scanning slit configuration can work equally well with a prism array, a hemispherical analyzer, or any other spectrometer, provided that the spectrometer images the entrance plane onto an exit plane.

As a final description of the setup, we show a three-dimensional view of the energy filter in figure 7. Notice that in this figure the dual-lens objective system has been represented by a single objective lens. In the entrance plane to the prism array, coinciding with the backfocal plane of the objective lens, the Ewald spheres for different electron energy are concentric, centered around the optical axis. An entrance slit selects a narrow horizontal slice, which enters the prism array. On passing through the prism array, this slice gets dispersed, with higher energy electrons experiencing a smaller total deflection angle that lower energy electrons. In the exit plane of the prism array, corresponding to a conjugate backfocal plane, the energy spectrum is in focus, and a contrast aperture can be used to select the electron energy desired for energy filtered image formation. Alternatively, the entrance slit can be scanned in the vertical direction, and an energy spectrum recorded for each slit position. From such a dataset a full E–k distribution can be obtained. In section 4 we will present examples of these various modes of operation.

4. Experimental results

Here we will present several initial results obtained with the prism array energy filter. First, let us look at the energy resolution. Figure 8 shows a composite figure of k_y versus E energy spectra, obtained with incident electron energies of ~5, 10, 15, 20, 25 and 30 eV scattering from an oxidized Si wafer. The microscope was operated at an electron gun energy of 10 keV. Immediately we recognize the parabolic envelope of the spectra. On the high energy side of the spectra we see a bright line, due to elastically scattered electrons. Electrons that have lost energy are to the left of these bright lines. As the sample potential is increased, the landing energy of the electrons also increases, but after re-acceleration the reflected elastic electron energy remains constant. Thus, the bright elastic electron energy line stays in the same place, and the parabolic k_y versus E distribution 'grows' to the left.

An electron energy spectrum can be obtained by taking a cut through the center of the spectrum. Such a cut is shown in figure 9, where we measure a full width at half maximum (fwhm) of the elastic peak of 0.33 eV. This peak width is a convolution of the energy distribution of the electrons generated by the cold field emission gun, and the energy resolution of the prism array energy filter. Assuming a reasonable energy spread of the cold field emission gun [12] of 0.25–0.3 eV, we obtain a spectrometer resolution of 0.15–0.20 eV, at a pass energy of 10 keV, or a resolving power

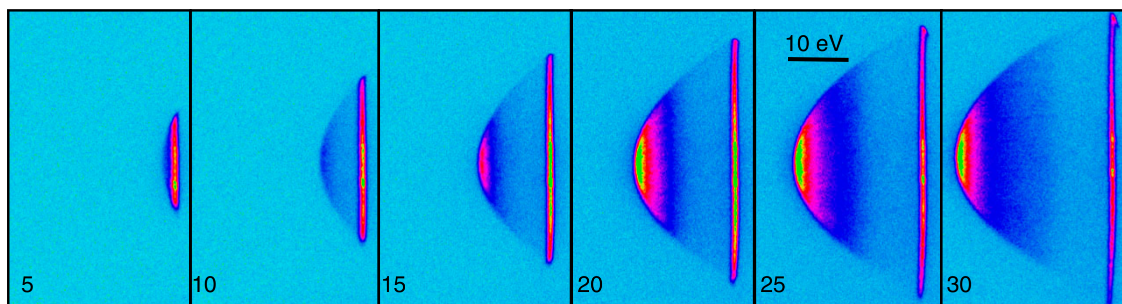

Figure 8. Electron energy spectra obtained with 5, 10, 15, 20, 25 and 30 eV electrons impinging on an oxidized Si wafer. The elastic peak (zero energy loss, highest kinetic energy) shows up as the bright line on the right-hand side of each spectrum. The parabolic (k_y, E) distribution is clearly seen, with the low energy secondary electrons (lower kinetic energy) on the left-hand side of each parabola. The secondary electron intensity increases with increasing incident electron energy.

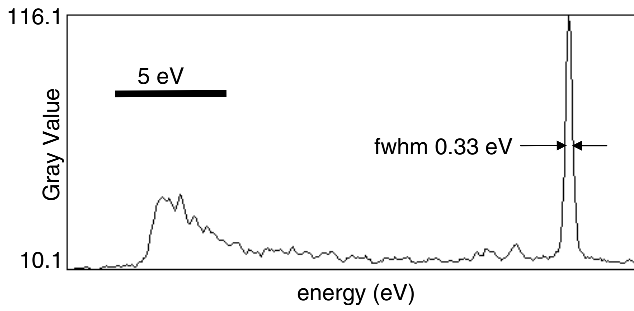

Figure 9. High resolution energy spectrum obtained by taking a slice through an electron energy spectrum such as shown in figure 8. The intense peak at the high energy side is the elastic peak, which has a measured width of 0.33 eV. This width is a convolution of the energy distribution of the electron gun (0.25–0.3 eV), and the resolution of the spectrometer. From this, we estimate a resolution $\Delta E/E \leqslant 2 \times 10^{-5}$.

$\Delta E/E < 2 \times 10^{-5}$, without deceleration of the electrons on their path through the spectrometer. This compares very favorably with results obtained with the omega energy filter in the SMART system, which has obtained a virtually identical resolving power [13].

Figure 10(a) shows an (k_y, E) energy spectrum, obtained at a full beam energy of 10 keV, reflected from a Si(111) sample onto which Ag islands were grown inside the LEEM system [14]. The landing energy of the electrons on the sample was 19 eV. The spectrum, obtained from the island area shown in figure 10(b), shows an intense elastic peak, and on the low energy side a weak Ag plasmon loss peak is observed. The momentum dispersion or the plasmon loss peak is clearly observed, and in good agreement with previous results [14]. Data acquisition time of this spectrum was 1 s. The entrance slit had a width of 1.5 μm, corresponding to an energy resolution of 0.16 eV at the 10 keV beam energy used here. The full width at half maximum of the no-loss peak is 0.30 eV, in good agreement with the expected resolution. The width of the plasmon loss peak is 0.37 eV. Notice that for this experiment, both the incident and reflected electron beams pass through the 1.5 μm entrance slit. Replacing the high resolution 1.5 μm energy slit with a wider band-pass slit of 20 μm (2.2 eV width), energy filtered images (of a different island) were recorded with elastically scattered electrons (figure 11(d)). This is a composite Ag island, with the bright area corresponding to Ag(111), and the dark area towards the right corresponding to Ag(001). We find such composite islands are not unusual, and the orientation can be conveniently established by selected area low energy electron diffraction. In this no-loss image, obtained at an electron energy of 52 eV, atomic steps are clearly resolved. The no-loss intensity from the Ag(111) area is much stronger than from the Ag(001) area. This intensity is simply related to the (0, 0) normal incidence LEED beam intensity at that energy, and both the absolute and relative intensities change with the landing energy of the electrons. Additional images were obtained with energy filtered plasmon loss electrons at an incident electron energy of 33 eV (figure 11(e)), and 52 eV (figure 11(f)). In these plasmon loss images, the loss intensity on Ag(111) and Ag(001) scales with the elastic scattering intensity in the (0, 0)

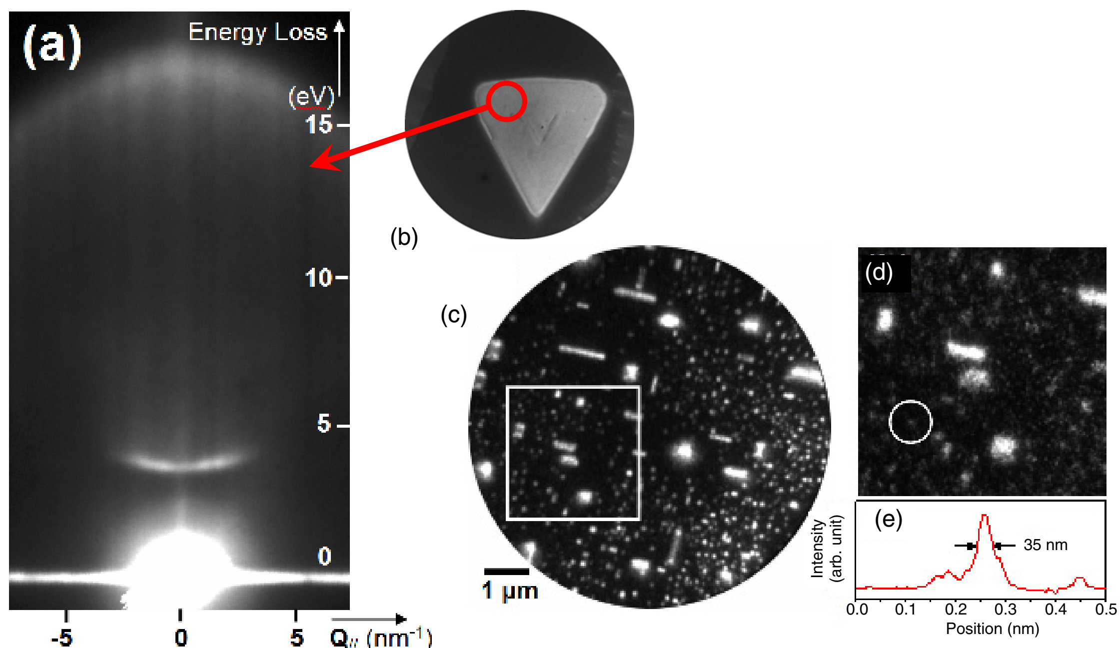

Figure 10. (a) A typical electron energy loss spectrum obtained from a Ag(111) island with an electron landing energy of 19 eV. The slit is parallel to the Γ–M direction. Elastically scattered electrons form a bright band at $E_{\mathrm{loss}} = 0$, with the specular beam at $Q_{\parallel} = 0$. A surface plasmon loss feature is seen at 3.7–4.0 eV with noticeable dispersion. (b) Hg PEEM image of Ag(111) island grown on Si(111), indicating the area from which the spectrum shown in (a) was obtained. (c) Hg PEEM image of Ag nanowires grown on Si(001) of Ag nanowires on Si(001). (d) Plasmon loss image of Ag nanowires (electron landing energy 81 eV). The observation area is shown as a solid square in (c). (e) One of the Ag nanoclusters marked by a solid circle in the surface plasmon loss LEEM image has a fwhm of 35 nm, close to the typical size of these clusters as measured with AFM.

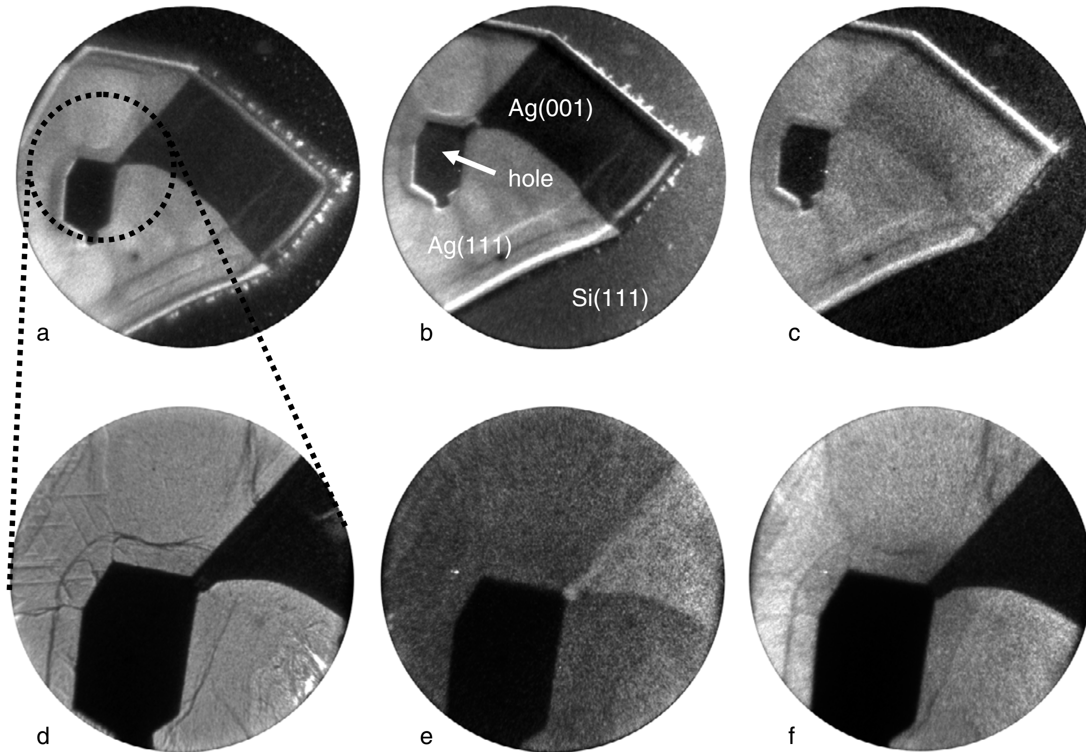

Figure 11. (a) Hg PEEM image of a Ag island grown on Si(111). The bright area corresponds to Ag(111), while the darker rectangular area on the right corresponds to Ag(001). The hexagonal feature left of center is a small hole in the island. (b) Secondary electron image, obtained using He I (21.2 eV) irradiation, and 20 μm entrance slit and contrast apertures. (c) Image obtained under the same conditions as (b), but now selecting d-electrons instead of secondary electrons (see also figure 12). Field of view 16 μm. (d) No-loss LEEM image, obtained at an incident electron energy of 52 eV. (e) Plasmon loss image, obtained at an incident electron energy of 33 eV. (f) Plasmon loss image, obtained at an incident electron energy of 52 eV.

beam, as expected. The plasmon loss feature is observed only on the Ag island, and not on the surrounding Si substrate. These are the first plasmon loss images reported with LEEM to date [14]. We were also able to obtain plasmon loss images on Ag nanowires grown on Si(001). Figure 10(c) shows a Hg PEEM image of such nanowires, while a plasmon loss image (obtained at an electron landing energy of 81 eV) of the area marked in figure 10(c) is shown in figure 10(d). A linescan through one of the smallest features in this images demonstrates a spatial resolution of <35 nm.

An illustrative set of energy resolved PEEM results were also obtained on these same epitaxial Ag islands [15]. Figure 11(a) shows a Hg PEEM image. Figure 11(b) shows an image obtained with secondary electrons generated by He I (21.2 eV) irradiation, very similar to the image of figure 11(a). Both images display the Ag(111) area with bright contrast, while the Ag(001) area is dark. One may be tempted at first to ascribe the contrast difference between the brighter (111) and darker (001) regions of the island to a difference in workfunction, with Ag(001) having a higher workfunction than Ag(111), so that the Hg photon energy is insufficient to generate photoelectrons from the (001) area. But such an explanation proves incorrect, as the (111) and (001) workfunction are virtually identical. Instead, it turns out that while on the Ag(111) surface a final state band is readily available for Hg excited photoelectrons, this is not the case for Ag(001) [15]. Such final state effects are well known from photoemission studies on these surfaces, although they are not often considered in PEEM imaging. Selecting the Ag d-band at a binding energy of 5–6 eV with the energy filter, we obtain the image in figure 11(c), where the contrast difference between Ag(111) and Ag(001) is only small. Imaging of surfaces with He I and He II radiation requires a discharge light source that is significantly brighter than the typical standard discharge lamp. In these experiments we used a SPECS UV-300 lamp equipped with an elliptical focusing capillary that images the discharge region in the lamp onto the surface, increasing brightness by about a factor 50. Without this focusing capillary the experiments reported there would be all but impossible.

We can obtain not only energy filtered real-space images, but also energy filtered dispersion data. Figure 12(b) shows an energy versus k_y data set obtained by imaging the dispersive plane with the entrance slit placed across the center of the Ewald sphere, with a selected area aperture located on a 3 μm diameter area of the Ag(111) part of the island. Similar data are shown on the Ag(001) area in figure 12(c). The dispersion of the Ag d-bands is readily observed. By scanning the filter entrance aperture across the Ewald sphere we can reconstruct the full 3D k_x–k_y–E dispersion figures for these selected areas, as shown in figure 13 for both Ag(111) (b) and Ag(001) (c). For the Ag(001) data, the data were 4-fold averaged, and for Ag(111) 3-fold averaged. While the slit step size was

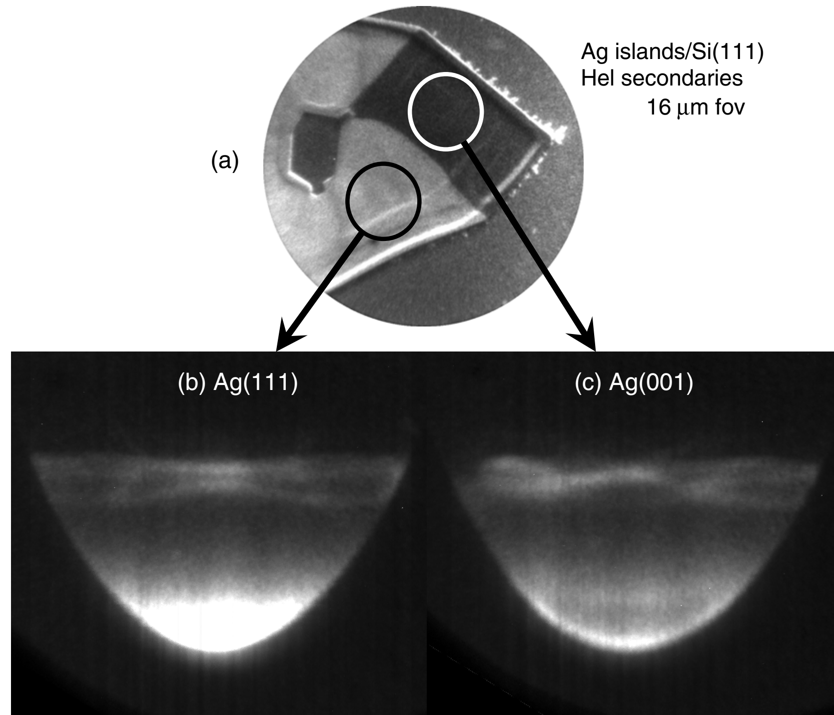

Figure 12. (k_y, E) spectra obtained on the Ag island shown in figure 11. The entrance slit is placed at $k_x \approx 0$. The d-band dispersions in (b) and (c) are significantly different, reflecting the different symmetries of these two crystal orientations.

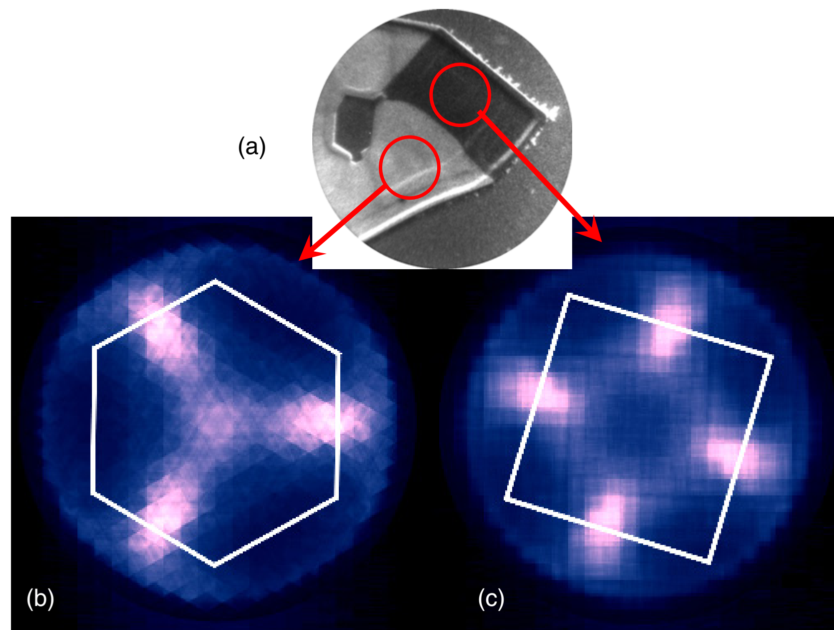

Figure 13. d-band maps for Ag(111) (b) and Ag(001) (c), at a binding energy of ~5.5 eV. The pronounced 3- or 4-fold maxima correspond to a direct occupied–unoccupied transition at the bulk L point [15].

rather coarse in these experiments, the pronounced difference in the d-band dispersion between these two surfaces stands out vividly. We believe that this is the first time that such detailed dispersion data were obtained on such microscopic surface areas without making use of synchrotron radiation [15].

Finally, we show results obtained on 1.5 ML of graphene grown inside the LEEM on a SiC(0001) substrate [16]. Again, a full E–k dataset was obtained by scanning the slit across the Eward sphere. Raw data (no averaging applied) are presented in figure 14, which shows k_y–E data as the entrance slit is scanned. The higher energy part of the spectra are due to He II excitation (photon energy 40.8 eV), while the lower energy part is due to both He I excitation (21.2 eV) and He II excitation. The upper He II part of the spectrum shows very pronounced

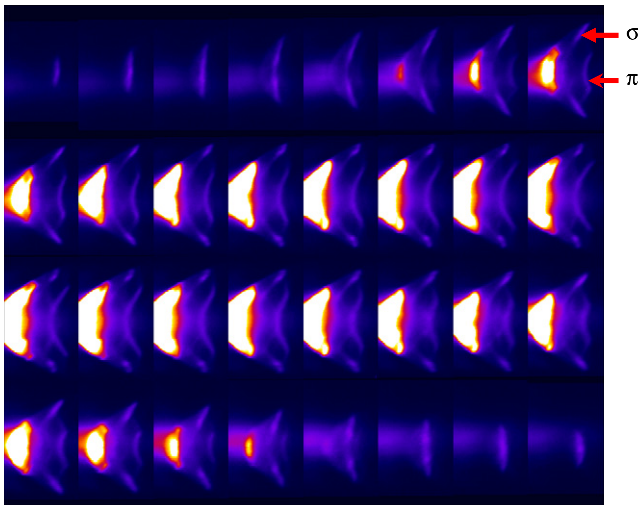

Figure 14. Set of energy spectra obtained on 1.5 ML of graphene grown on SiC(0001) by high temperature annealing in vacuum. This sequence of (k_y, E) spectra (running from top left to bottom right) was obtained by scanning the slit through the entrance side backfocal plane and recording a spectrum for each setting. The sample was simultaneously illuminated with He I (21.2 eV) and He II (40.8 eV) UV light obtained from a focused SPECS UV-300 He discharge source. In the He II part of the spectrum, the graphene σ and π bands are easily recognized (see arrows). Raw data are shown.

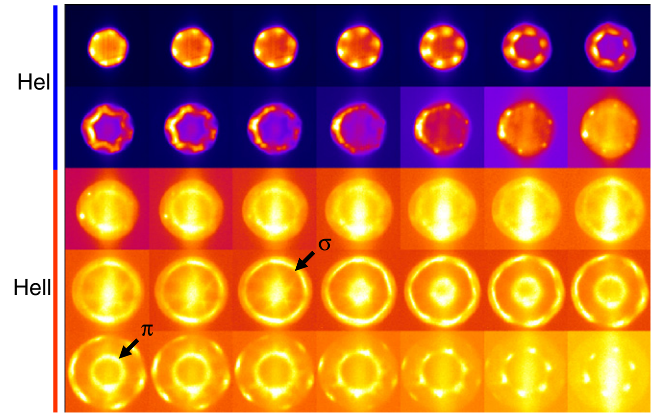

Figure 15. Energy resolved (k_x, k_y) maps extracted from the data shown in figure 14. The top two rows are predominantly due to the He I UV light illumination. The most right-hand frame in the second row shows 6 discrete spots, corresponding to the graphene Dirac points. In the He II part of the figure, the graphene σ and π bands are easily distinguished, as are the Dirac points in the final frame. The maps are separated by 0.98 eV between frames. Raw data are shown.

π and σ bands due to the graphene film [17]. By slicing the E–k paraboloid along planes of fixed energy, we obtain a set of k_x–k_y (E) figures, i.e. the azimuthal distribution of the photoelectron intensity as a function of electron energy. A composite of such figures is shown in figure 15, which vividly illustrates the strong energy dependence of the electron wavevector distribution, i.e. the 3D bandstructure of the thin graphene layer. Figures 14 and 15 contain about 20% of the full dataset, which was obtained in a lab setting, using a focused He light source, in about an hour measurement time.

5. Transmission and resolution

A question that we have so far not addressed is that of transmission and resolution. Let us address the second issue first. We must distinguish between spatial and energy resolution. In spectroscopy mode (displaying energy spectra, as well as energy filtered diffraction patterns), the energy resolution for a sufficiently small field of view is determined by the width of the entrance slit on the objective lens side of the prism array. At 15 keV electron energy the dispersion is 6 μm eV^{-1}, i.e. a slit with a width of 1 μm gives rise to an energy resolution of 0.16 eV. Results obtained on Ag islands (see above) indicate that we indeed obtain an energy resolution at this basic limit. Another limitation on the available energy resolution comes from the non-isochromaticity of the energy filter. If we insert an energy filter slit on the entrance slit of the analyzer, we observe a dispersed energy spectrum on the exit side. Ideally, if we now use a contrast aperture to select a small energy window in the dispersed energy spectrum, an image formed with this selection aperture would be constant in energy across the full image, i.e. the image is isochromatic across the field of view. But most energy filters are not ideal, and there is a linear gradient of energy versus position across the image. Using a hemispherical analyzer, this non-isochromaticity can reach 1 or more eV per 10 μm. For the prism array used in this work, the measured non-isochromaticity is 0.5 eV/10 μm. The inverse also holds: if we select electrons from a finite sample area, using a selected area aperture on the diagonal plane of the prism, a sharp line in the energy spectrum will be broadened in the energy dispersive plane. If we use a selected area of 10 μm, then the energy resolution can be no better than 0.5 eV in the present case. So for the highest energy resolution experiments one needs to restrict the sample area from which the electrons are analyzed so as to not unnecessarily deteriorate the energy resolution in the electron energy spectra. This is a significant factor. With a non-isochromaticity of 0.05 eV μm^{-1} (as in the present setup), and a desired energy resolution of 0.15 eV, the largest area that can be selected using a selected area aperture is 3 μm in diameter. For a more typical non-isochromaticity of 0.1 eV μm^{-1}, this reduces to just 1.5 μm, a reduction in transmission by a factor 4.

In many angle resolved photoemission experiments one is interested in obtaining valence band dispersions along specific high symmetry direction in the surface or bulk Brillouin zone. As the data in figures 12 and 14 show, such data can be obtained very rapidly by aligning the entrance slit with the plane of interest, and recording the corresponding energy and momentum resolved spectrum. To make this fully flexible, so that any plane through the Brillouin zone can be selected for spectroscopy, it is desirable that the sample stage have an azimuthal degree of freedom, allowing the Brillouin zone to be rotated relative to the orientation of the entrance slit. The IBM LEEM/PEEM instrument in its current configuration does not have this azimuthal rotation. However, a new sample stage incorporating azimuthal rotation is presently in development. An alternative solution would be to control the azimuthal rotation with the transfer lens located between the objective

lens and the entrance slit. This is now a magnetic lens with a fixed rotation angle of $\sim 60^\circ$. It is possible in principle to replace this lens with a combined magnetic/electrostatic lens, where the desired focal length can be obtained by varying the ratio of magnetic to electrostatic excitation. This would allow for a rotation range of $\pm 60^\circ$, sufficient to access any azimuthal plane of interest. The advantage of such a transfer lens would be its non-mechanical nature, simplifying the design of the sample stage. On the other hand, integrating both electrostatic and magnetic lens elements in a single, compact design without shifting the principle planes when varying the excitation ratio, poses its own challenges and is not pursued at the present time.

As to spatial resolution, we must distinguish between k-space and real space. K-space resolution will be limited in one direction by the width of the energy selection slit. In the other direction it will be limited by the quality of the backfocal plane image. Using LEED, we can obtain diffraction spots with a width of ~ 0.002 Å^{-1} which sets the fundamental limit. A slit width of 1.5 μm corresponds to a k width of 0.02 Å^{-1}. In real space, the image resolution will be limited both by the diameter of the energy selection aperture below the prism array (contrast aperture), and by the corresponding energy window ΔE. At least three factors contribute to spatial resolution. The first is diffraction. Image blurring due to diffraction varies with $1/\alpha$, where α is the angular width accepted by the contrast aperture. As the aperture angle becomes larger, this contribution to the resolution will decrease. On the other hand, chromatic aberration increases linearly with $C_c \alpha \Delta E/E$, where C_c is the chromatic aberration coefficient of the objective lens, and spherical aberration with $1/2 C_s \alpha^3$, where C_s is the spherical aberration coefficient. In addition, higher order aberration coefficients may be significant. In general, there will be an optimum aperture angle α for which the resolution is at a minimum for a given energy spread ΔE. For $\Delta E =$ 1.5 eV (3 eV average electron energy leaving the sample), the theoretical spatial resolution is ~ 13 nm. For an energy window of 0.5 eV, this would be closer to 20 nm, limited by diffraction. If an aberration corrector is included in the microscope (a project that we are currently working on), an energy window $\Delta E = 3$ eV, for 10 eV electrons leaving the sample, will result in a spatial resolution of ~ 4 nm [18].

Often, one would like to have higher resolution energy spectra on selected areas of the sample. This can be accomplished by utilizing an appropriate selected area aperture in the image (placed in the diagonal plane of the prism array), and acquiring an energy spectrum for that selected area. Obtaining images with higher energy resolution suffers from the problem—with *any* energy filter—that transmission rapidly drops as the energy window ΔE is decreased. Transmission is therefore critical. Using the setup as described here, transmission is straightforward to understand. All electrons selected by the entrance slit to the prism array are transmitted with a probability of one as they are dispersed into the exit plane. The sample area from which electrons can be collected for a given desired energy resolution is limited by non-isochromaticity. Thus, lower non-isochromaticity leads to higher overall transmission.

In any energy filter, one must make a tradeoff between energy dispersion and spatial resolution. For a contrast aperture with diameter δ, the angular aperture is given by $\delta = c\alpha$. The value of c depends on the magnification of the diffraction plane. At the same time, the aperture diameter δ corresponds to a selected energy window ΔE by $\Delta E = \delta/D$, where D is the dispersion of the spectrometer (in μm eV^{-1}). Thus, the energy window ΔE is related to aperture angle and dispersion by $\Delta E = c\alpha/D$. For a higher dispersion D, a given aperture angle α will select a narrower energy range ΔE. Of course, the narrower the energy window ΔE, the lower the transmission. Conversely, with a lower dispersion D, a given aperture angle α will select a wider energy range ΔE, increasing transmission, but limiting the energy resolution of the image. In many if not most cases, image acquisition in energy filtered PEEM is limited by signal strength, i.e. there are not a lot of photoelectrons to work with. In that case it is best to select an energy window ΔE that transmits all the electrons in a given photoemission peak (core level, valence band feature, etc). Such peaks typically have a width of 1–3 eV, and the strongest signal is obtained when this signal is fully transmitted. The energy width ΔE must then be matched to the natural energy width of the signal, without sacrificing spatial resolution. This is accomplished in the present design, where ΔE and spatial resolution are naturally matched by the intrinsic dispersion of the spectrometer. Obtaining energy filtered images with an energy resolution that is higher than the intrinsic width of the photoemission peaks is not useful, as it unnecessarily reduces transmission without the benefit of increased information. High energy resolution photoelectron spectra can always be obtained with a selected area aperture in spectroscopy mode, in which case the low non-isochromaticity of 0.05 eV μm^{-1} helps to optimize transmission. Very high dispersion can be useful only when signal intensity is not an issue, a situation rarely encountered.

Finally, let us comment on the use of synchrotron radiation in PEEM experiments. In most instances, elemental specificity in these experiments is obtained by tuning the photon energy to a core level absorption structure characteristic of the element of interest. The PEEM instrument is usually set up to detect low energy (<10 eV) secondary electrons. To obtain the best signal level, it is advantageous to transmit a wide energy window in this secondary electron band. Using the prism array as an energy filter, we can easily transmit a 3 eV wide energy window, allowing for high transmission as well as high spatial resolution, while high spectroscopic image resolution is guaranteed by the high energy resolution of the illuminating synchrotron photon beam. In this very typical experiment, a narrow pass band (i.e. high energy resolution) in the electron spectrometer is a decided disadvantage, as it unnecessarily reduces transmission, without resulting in either higher spatial or spectroscopic resolution. With the inclusion of an aberration corrector in the microscope column, we predict a spatial resolution of better than 4 nm in such an experimental setup [18].

6. Conclusions and outlook

We have introduced a new in-line energy filter for a LEEM/PEEM system, utilizing the prism array that is an

integral part of the microscope as a versatile and simple dispersive element that can be used to obtain energy filtered images, energy filtered photoelectron momentum distributions, as well as full energy resolved E–k data. It is a distinct advantage of the present design that introduction of the energy filter function does not lead to an increase in the number of electron optical components or electron optical complexity. Utilizing the energy filter only requires the insertion of the energy filter entrance slit in the diffraction plane at the objective lens side of the prism array, without additional complications in microscope alignment. We have shown a range of experimental results, demonstrating an energy resolution $\Delta E/E = 2 \times 10^{-5}$, comparable with the highest resolution spectrometers available today [13]. Using a focused lab-based He I/He II light source we have obtained the first full valence band spectroscopic data in any LEEM/PEEM not coupled to a synchrotron light source, with very modest data acquisition times, even on sample areas of just a few square micrometers [15]. We have also presented the first electron energy loss plasmon dispersion data, and the first energy filtered plasmon loss images obtained with LEEM to date [14]. The simplicity of the design, combined with the robustness of operation, and the wide flexibility of imaging and spectroscopy modes makes this design particularly attractive. Future addition of an aberration corrector, eliminating both chromatic and spherical aberration, will enable spectroscopic photoemission imaging with spatial resolution as high as 4 nm, and LEEM imaging with a spatial resolution below 1.5 nm [18].

In addition to the focused He I/He II discharge lamp, laser-based light sources are becoming increasingly available [19, 20]. Rather than bringing the microscope to the light source, it is now becoming possible to bring the light sources to the microscope, and to perform powerful spectromicroscopy and microspectroscopy experiments in a traditional laboratory environment. This will broaden and deepen the impact that LEEM/PEEM will have in physics, materials science, as well as bio and medical sciences.

Acknowledgments

We thank Dr Marian Mankos for the calculations of the prism array optical properties presented here. We also acknowledge the encouragement and support of Professor Toshio Sakurai (Tohoku University, Sendai, Japan). Finally, we like to express our gratitude to Professor Ernst Bauer, for his support and encouragement of the LEEM program at IBM since its inception 20 years ago, and for his efforts to foster and maintain a spirit of openness and collegiality in the LEEM/PEEM community, as exemplified by the wonderful workshop of which this volume forms a record. We all wish you a happy 80th birthday!

References

[1] See in particular Rose H and Krahl D 1995 *Energy-Filtering Transmission Electron Microscopy* (*Springer Series in Optical Sciences*) ed R Ludwig (Berlin: Springer) chapter 4 (Electron Optics of Imaging Filters)
[2] Griffith O H and Engel W 1991 *Ultramicroscopy* **36** 1–28
Bauer E, Mundschau M, Sweich W and Telieps W 1989 *Ultramicroscopy* **31** 49–57
Tromp R M and Hannon J B 2002 *Surf. Rev. Lett.* **9** 1565–93
Hannon J B and Tromp R M 2003 *Annu. Rev. Mater. Res.* **33** 263–88
[3] For information on the Gatan Image Filter, see www.gatan.com
[4] Veneklasen L H 1992 *Rev. Sci. Instrum.* **63** 5513 and references therein
[5] Abbati I, Braicovich L and De Michelis B 1972 *J. Phys. E: Sci. Instrum.* **5** 627 and references therein
[6] See for instance Kiss T, Kanetaka F, Yokoya T, Shimojima T, Kanai K, Shin S, Onuki Y, Togashi T, Zhang C, Chen C T and Watanabe S 2005 *Phys. Rev. Lett.* **94** 057001
[7] Renault O, Barrett N, Bailly A, Zagonel L F, Mariolle D, Cezar J C, Brookes N B, Winkler K, Krömker B and Funnemann D 2007 *Surf. Sci.* **601** 4727–32
[8] Preikszas D and Rose H 1997 *J. Electron Microsc.* **46** 1
Rose H and Preikszas D 1992 *Optik* **92** 31
[9] Kolarik V, Mankos M and Veneklasen L 1991 *Optik* **87** 1
[10] Rose H, Degenhardt R and Preikszas D 1994 *US Patent Specification* 5,319,207 (June 7)
[11] Tromp R M, Mankos M, Reuter M C, Ellis A W and Copel M 1998 *Surf. Rev. Lett.* **5** 1189
Tromp R M, Mankos M, Reuter M C, Ellis A W and Copel M 1998 unpublished
[12] Young R D and Müller E W 1959 *Phys. Rev.* **113** 115
Kimoto K, Ishizuka K, Asakai T, Nagai T and Matsui Y 2005 *Micron* **36** 465
[13] Marchetto H 2006 High-resolution spectro-microscopic investigations of organic thin film growth *Doctoral Thesis* Berlin www.diss.fu-berlin.de/2006/458/
[14] Fujikawa Y, Sakurai T and Tromp R M 2008 *Phys. Rev. Lett.* **100** 126803 and references therein
[15] Fujikawa Y, Sakurai T and Tromp R M 2009 *Phys. Rev.* B **79** 121401
[16] Hannon J B and Tromp R M 2008 *Phys. Rev.* B **77** 241404
[17] See for instance Geim A K and Novoselov K S 2007 *Nat. Mater.* **6** 183–91 and references therein
[18] Tromp R M *et al* 2009 unpublished
[19] Meyer zu Heringdorf F-J, Chelaru L I, Möllenbeck S, Thien D and Horn von Hoegen M 2007 *Surf. Sci.* **601** 4700–5
Nakagawa T, Yokoyama T, Hosaka M and Katoh M 2007 *Rev. Sci. Instrum.* **78** 023907
[20] Chen C T, Kanai T, Wang X Y, Zhu Y and Watanabe S 2008 *Opt. Lett.* **33** 202
Gibson E A, Paul A, Wagner N, Tobey R, Gaudiosi D, Backus S, Christov I P, Aquila A, Gullikson E M, Attwood D T, Murnane M M and Kapteyn H C 2003 *Science* **302** 95